Journal of Computational Acoustics, Vol. 12, No. 1 (2004) 1–21

INTERNATIONAL ASSOCIATION
FOR MATHEMATICS AND
COMPUTERS IN SIMULATION

SIMULATION OF WAVES IN PORO-VISCOELASTIC ROCKS SATURATED BY IMMISCIBLE FLUIDS. NUMERICAL EVIDENCE OF A SECOND SLOW WAVE

JUAN ENRIQUE SANTOS* and CLAUDIA LEONOR RAVAZZOLI†

CONICET, Departamento de Geofísica Aplicada,
Facultad de Ciencias Astronómicas y Geofísicas,
Universidad Nacional de La Plata, Paseo del Bosque S/N, La Plata (1900) Argentina
**santos@fcaglp.fcaglp.unlp.edu.ar*
†*claudia@fcaglp.fcaglp.unlp.edu.ar*

PATRICIA MERCEDES GAUZELLINO

Departamento de Geofísica Aplicada, Facultad de Ciencias Astronómicas y Geofísicas,
Universidad Nacional de La Plata, Paseo del Bosque S/N, La Plata (1900) Argentina
gauze@fcaglp.fcaglp.unlp.edu.ar

JOSE M. CARCIONE‡ and FABIO CAVALLINI§

Istituto Nazionale di Oceanografia e di Geofisica Sperimentale (OGS),
Borgo Grotta Gigante 42c, 34010 Sgonico, Trieste, Italy
‡*jcarcione@ogs.trieste.it*
§*fcavallini@ogs.trieste.it*

Received 15 November 2002
Revised 14 February 2003

We present an iterative algorithm formulated in the space-frequency domain to simulate the propagation of waves in a bounded poro-viscoelastic rock saturated by a two-phase fluid. The Biot-type model takes into account capillary forces and viscous and mass coupling coefficients between the fluid phases under variable saturation and pore fluid pressure conditions. The model predicts the existence of three compressional waves or Type-I, Type-II and Type-III waves and one shear or S-wave. The Type-III mode is a new mode not present in the classical Biot theory for single-phase fluids. Our differential and numerical models are stated in the space-frequency domain instead of the classical integrodifferential formulation in the space-time domain. For each temporal frequency, this formulation leads to a Helmholtz-type boundary value problem which is then solved independently of the other frequency problems, and the time-domain solution is obtained by an approximate inverse Fourier transform. The numerical procedure, which is first-order correct in the spatial discretization, is an iterative nonoverlapping domain decomposition method that employs an absorbing boundary condition in order to minimize spurious reflections from the artificial boundaries. The numerical experiments showing the propagation of waves in a sample of Nivelsteiner

*Also Department of Mathematics, Purdue University, 150 N. University Street, West Lafayette, Indiana, 47907-2067, USA.

sandstone indicate that under certain conditions the Type-III wave can be observed at ultrasonic frequencies.

Keywords: Poroviscoelasticity; finite elements; multiphase fluids; wave propagation.

1. Introduction

The analysis of the variation of the seismic response of reservoir rocks as function of the properties of the saturant fluids under variable saturation and pressure conditions is an active area of research in exploration geophysics and reservoir engineering.

According to Biot's theory,[1–3] in a porous solid saturated by a single phase fluid, one shear or S-wave wave and two compressional waves (fast or Type I and slow or Type II) can propagate. The slow Biot mode has been detected in the laboratory,[4] and has been simulated, as a wave,[5–8] and as a quasi-static mode[9] by using numerical modeling.

Models to represent wave propagation in porous rocks with full, partial, multi-phase, or segregate fluid saturation have been presented by different authors,[2,3,10–14] but none of them take into account the pore fluid pressure and the capillary forces to obtain the coefficients of the constitutive relations and the viscous and mass coupling coefficients.

In this work, we use a generalized Biot model, which includes the effects of capillary pressure and the reference (absolute) pressures of the immiscible fluids on the stress–strain relations.[15,16] This model predicts the existence of three compressional waves or Type-I, Type-II and Type-III waves and one shear or S-wave. In the low frequency range, the Type-II and Type-III waves are slow diffusion-type waves, since viscous effects dominate. On the contrary, in the high-frequency range these waves become true propagating waves since inertial effects dominate, and for certain fluid pressure and saturations ranges both slow waves have phase velocities and attenuation factors of the same order of magnitude. These results led us to develop a numerical simulator to study the propagation of these waves.

Dispersion and attenuation of the different waves depend on several mechanisms, such as matrix viscoelasticity and viscous coupling between the fluid and the solid matrix. In the low frequency range, the viscous coupling coefficients are obtained from two-phase Darcy's law, and the high-frequency correction factors are defined as generalizations of the corresponding ones for the single-phase case (e.g. Ref. 17).

Viscoelastic dissipation is included by replacing the real-valued poroelastic coefficients in the constitutive relations by complex and frequency dependent poro-viscoelastic moduli satisfying the same relations as in the elastic case.

All these dissipative mechanisms, which are needed to represent the levels of attenuation observed in rocks,[13] are included by using mathematical models formulated in the space-frequency domain, which is difficult to implement in the space-time domain, where, in addition, the time history of the system needs to be stored in order to compute the solution at the current time using time convolutions. A different approach to avoid time convolutions by introducing memory variables is illustrated in Ref. 18 (see also Ref. 17).

In the space-frequency domain formulation, each temporal frequency problem can be solved independently of the other frequencies and then the space-time solution is obtained by an inverse Fourier transform.[19–24]

Numerical simulation of waves in porous media is computationally expensive due to the large number of degrees of freedom needed to calculate wave fields accurately. Use of a domain decomposition iteration is a convenient approach to overcome this difficulty. The type of nonoverlapping domain decomposition iteration used in this paper is presented in Ref. 25 for solving second-order elliptic problems. Nonconforming finite element spaces are introduced in Ref. 26 for the approximate solution of second order elliptic problems; the solution of the Helmholtz equation using this nonconforming space is analyzed in Ref. 22. Gauzellino *et al.*[24] illustrate a parallel implementation of a domain decomposition iteration, for computing wave fields in 2D and 3D attenuating media, using nonconforming finite element spaces.

Our numerical procedure is a nonoverlapping domain decomposition iteration employing the nonconforming rectangular element defined in Ref. 26 to approximate the solid displacement vector. The displacement of the two fluid phases are approximated by using the vector part of the Raviart–Thomas–Nedelec mixed finite element space of zero order, which is a conforming space.[27,28]

The algorithm is used for the simulation of waves in a sample of Nivelsteiner sandstone[29] saturated with gas and water, perturbed by a point source at ultrasonic frequencies to generate the wavefields. We show snapshots and traces (time histories) of the generated wavefields, where the events associated with the four different types of waves can be clearly observed.

2. The Model

We consider a porous solid saturated by two immiscible fluids. In this case, we distinguish a *wetting* phase and a *nonwetting* one, which will be denoted with the subscripts (or superscripts) "w" and "n", respectively. Let $\mathbf{x} = (x, y, z)$ and $S_n = S_n(\mathbf{x})$ and $S_w = S_w(\mathbf{x})$ denote the averaged wetting and nonwetting fluid saturations, respectively, with S_{rn} and S_{rw} being the corresponding residual saturations, which physical significance is as follows. S_{rw} is the amount of wetting fluid that will always remain in the pore space even at very high capillary pressures when the wetting fluid is being displaced by the nonwetting fluid, i.e. during a drainage regime (S_{rw} is known as connate water in the case of water). On the other hand, if we are in a process of imbibition, i.e. when the nonwetting fluid is being displaced by the wetting fluid, we observe that at zero capillary pressure a certain amount of nonwetting fluid remains; this is the residual saturation of the nonwetting fluid, denoted by S_{rn}. At $S_n < S_{rn}$ the nonwetting phase ceases to flow.[30] We assume that the two fluid phases completely saturate the porous part of the bulk material so that $S_n + S_w = 1$. We further assume that we are in the funicular saturation regime, in which each fluid phase occupy a continuous network of tortuous (funicular) paths where simultaneous flow of both fluids is possible, so that $S_{rn} < S_n < 1 - S_{rw}$.[30–32]

Let $u^s = (u_i^s)$, $\tilde{u}^n = (\tilde{u}_i^n)$ and $\tilde{u}^w = (\tilde{u}_i^w)$, $i = 1, 2, 3$ denote the time Fourier transforms of the averaged displacement vectors of the solid, nonwetting and wetting phases, respectively, and let $\phi = \phi(\mathbf{x})$ denote the matrix effective porosity. Set $u^l = \phi(\tilde{u}^l - u^s)$, $\xi^l = -\nabla \cdot u^l$, $l = n, w$, and let $\varepsilon_{ij}(u^s)$ and $e_b = \varepsilon_{ii}(u^s)$ be the Fourier transforms of the strain tensor of the solid and its linear invariant, respectively. Also, set $u = (u^s, u^n, u^w)$.

2.1. *Elastic stress-strain relations*

Let τ_{ij}, $i, j = 1, 2, 3$, P_n and P_w denote the Fourier transforms of the infinitesimal changes in the stress tensor of the bulk material and the pressures of the wetting and nonwetting fluids, respectively, with respect to corresponding reference values $\bar{\tau}_{ij}$, $\bar{P}_n$, and $\bar{P}_w$ associated with the initial equilibrium state with corresponding nonwetting fluid saturation $\bar{S}_n$ and porosity $\bar{\phi}$. Recall that P_n and P_w are related through the capillary relation[30–32]

$$P_{ca} = P_{ca}(S_n + \bar{S}_n) = \bar{P}_n + P_n - (\bar{P}_w + P_w) = P_{ca}(\bar{S}_n) + P_n - P_w \geq 0\,. \tag{2.1}$$

Based on experimental data and ignoring hysteresis, the function P_{ca} is a positive and strictly increasing function of the nonwetting fluid saturation.

The stress-strain relations are derived in Ref. 15. With $\beta = P_{ca}(\bar{S}_n)/P'_{ca}(\bar{S}_n)$, $\zeta = \bar{P}_w/P'_{ca}(\bar{S}_n)$, here we state them in a form that includes the absolute reference pressure of the fluid phases:

$$\begin{aligned}
\tau_{ij}(u) &= 2N\varepsilon_{ij} + \delta_{ij}(\lambda_c e_b - B_1\xi^n - B_2\xi^w)\,,\\
\mathcal{T}_n(u) &= (\bar{S}_n + \beta + \zeta)P_n - (\beta + \zeta)P_w = -B_1 e_b + M_1\xi^n + M_3\xi^w\,,\\
\mathcal{T}_w(u) &= (\bar{S}_w + \zeta)P_w - \zeta P_n = -B_2 e_b + M_3\xi^n + M_2\xi^w\,.
\end{aligned} \tag{2.2}$$

The quantities τ_{ij}, $\mathcal{T}_n$ and $\mathcal{T}_w$ are the generalized forces of the system.

The coefficient N is the shear modulus of the dry rock (i.e. $N = N_m$), while $\lambda_c = K_c - (2/3)N$ in 3D and $\lambda_c = K_c - N$ in 2D, with K_c being the undrained bulk modulus. Following Ref. 16 $K_c = K_c(\mathbf{x})$ is computed using the formulae

$$\begin{aligned}
K_c &= K_s(K_m + \Xi)/(K_s + \Xi)\,, \qquad \Xi = K_f(K_m - K_s)/\bar{\phi}(K_f - K_s)\,,\\
K_f &= \alpha(\gamma\bar{S}_n C_n + \bar{S}_w C_w)^{-1}\,, \qquad \alpha = 1 + (\bar{S}_n + \beta)(\gamma - 1)\,,\\
\gamma &= (1 + P'_{ca}(\bar{S}_n)\bar{S}_n\bar{S}_w C_w)(1 + P'_{ca}(\bar{S}_n)\bar{S}_n\bar{S}_w C_n)^{-1}\,,
\end{aligned} \tag{2.3}$$

where $K_m(\mathbf{x})$, $K_s(\mathbf{x})$, K_n and K_w are the bulk modulus of the empty matrix, the solid grains and the nonwetting and wetting fluid phases, respectively, with corresponding compressibilities $C_l = K_l^{-1}$, $l = m, s, n, w$.

The remaining coefficients can be obtained by using the following relations:

$$B_1 = \chi K_c[(\bar{S}_n + \beta)\gamma - \beta + (\gamma - 1)\zeta]\,, \quad B_2 = \chi K_c[(\bar{S}_w + (1 - \gamma)\zeta]\,, \tag{2.4}$$

$$M_1 = -M_3 - B_1 C_m\delta^{-1}\,, \quad M_2 = (rB_2 + \zeta)q^{-1}\,, \quad M_3 = -M_2 - B_2 C_m\delta^{-1}\,, \tag{2.5}$$

with

$$\chi = [\delta + \bar{\phi}(C_m - C_c)]\{\alpha[\delta + \bar{\phi}(C_m - C_f)]\}^{-1}\,, \quad q = \bar{\phi}(C_n + 1/P'_{ca}(\bar{S}_n)\bar{S}_n\bar{S}_w)\,,$$

$$r = (\bar{S}_n + \beta)C_s + (C_c - C_m)[qB_2 + (\bar{S}_n + \beta)(1 - C_s C_c^{-1})]\,, \quad \delta = C_s - C_m\,.$$

2.2. *Poro-viscoelastic moduli*

Besides viscous friction effects, which are described later, in order to model the levels of attenuation of waves travelling in real rocks we will also assume linear viscoelastic behavior for the bulk material using the correspondence principle as stated by Biot.[1,10,17] Thus we replace the real elastic moduli by viscoelastic operators in the space-time domain, so that in the space-frequency domain the elastic moduli in (2.2) become complex and frequency dependent.

In this work we will make the undrained bulk modulus K_c and the shear modulus N complex and frequency dependent, while all other coefficients in (2.2) are real. We use the linear viscoelastic model derived in Ref. 33:

$$K_c(\mathbf{x},\,\omega) = \frac{K_c^r(\mathbf{x},\,0)}{R_{K_c}(\mathbf{x},\,\omega) - iT_{K_c}(\mathbf{x},\,\omega)}\,, \quad N(\mathbf{x},\,\omega) = \frac{N^r(\mathbf{x},\,0)}{R_N(\mathbf{x},\,\omega) - iT_N(\mathbf{x},\,\omega)}\,. \tag{2.6}$$

The coefficients $K_c^r(\mathbf{x},\,0)$ and $N^r(\mathbf{x},\,0)$ denote the relaxed closed bulk and shear moduli, respectively. The frequency dependent functions $R_l(\mathbf{x})$ and $T_l(\mathbf{x})$, $l = K_c,\, N$, associated with a continuous spectrum of relaxation times, characterize the viscoelastic behavior and are given by[33,17]

$$R_l(\mathbf{x},\,\omega) = 1 - \frac{1}{\pi\hat{Q}_l(\mathbf{x})}\ln\frac{1+\omega^2T_{1,l}^2(\mathbf{x})}{1+\omega^2T_{2,l}^2(\mathbf{x})}\,, \quad T_l(\mathbf{x},\,\omega) = \frac{2}{\pi\hat{Q}_l(\mathbf{x})}\tan^{-1}\frac{\omega(T_{1,l}(\mathbf{x}) - T_{2,l}(\mathbf{x}))}{1+\omega^2T_{1,l}(\mathbf{x})T_{2,l}(\mathbf{x})}\,.$$

The model parameters $\hat{Q}_l(\mathbf{x})$, $T_{1,l}(\mathbf{x})$ and $T_{2,l}(\mathbf{x})$ are taken such that the quality factors $Q_l(\mathbf{x},\,\omega) = T_l(\mathbf{x})/R_l(\mathbf{x})$ are approximately equal to $\hat{Q}_l(\mathbf{x})$ in the range of frequencies where the equations are solved. The almost constancy of the quality factor versus frequency makes this model convenient for geophysical applications.

2.3. *The equations of motion for the full frequency range*

The equations of motion stated in the space-frequency domain, with ω denoting the angular frequency, are[15]:

$$-\omega^2(\rho u^s + \rho_n\bar{S}_n u^n + \rho_w\bar{S}_w u^w) - \nabla\cdot\tau(u) = f^s\,, \tag{2.7}$$

$$-\omega^2(\rho_n\bar{S}_n u^s + g_n u^n + g_{nw}u^w) + i\omega d_n u^n - i\omega d_{nw}u^w + \nabla\mathcal{T}_n(u) = f^n\,, \tag{2.8}$$

$$-\omega^2(\rho_w\bar{S}_w u^s + g_{nw}u^n + g_w u^w) + i\omega d_w u^w - i\omega d_{nw}u^n + \nabla\mathcal{T}_w(u) = f^w\,. \tag{2.9}$$

The coefficients ρ_n, ρ_w are, respectively, the mass densities of the nonwetting and wetting fluids, and ρ denotes the mass density of the bulk material given by $\rho = (1-\bar{\phi})\rho_s + \bar{\phi}(\bar{S}_n\rho_n + \bar{S}_w\rho_w)$, where ρ_s is the mass density of the solid grains.

The mass coupling coefficients g_n, g_w, g_{nw} represent the inertial effects associated with dynamic interactions between the three different phases, while the coefficients d_n, d_w and d_{nw} include the viscous coupling effects between the solid and fluid phases. It

is known that for single-phase fluids, in the high-frequency range, the viscous and mass coupling coefficients become frequency dependent.[3,34,17] This effect is associated with the departure of the flow from the laminar Poiseuille type at the pore scale, which occurs for frequencies greater than some characteristic value. Since we have two immiscible fluids flowing in the pore space and three relative permeability functions, following Ref. 11, we define three characteristic frequencies of the form $\omega_c^l(\bar{S}_n) = \bar{S}_l\mu_l\bar{\phi}\mathcal{A}_l/(\mathcal{G}\rho_l)$, $l = n, w$, $\omega_c^{nw}(\bar{S}_n) = \bar{\phi}(\mu_n\mu_w)^{\frac{1}{2}}(\bar{S}_n\bar{S}_w)^{\frac{1}{2}}K_{rnw}/(\epsilon\mathcal{A}\mathcal{G}(\rho_n\rho_w)^{\frac{1}{2}})$. The factor $\mathcal{G} = \mathcal{G}(\mathbf{x})$ is known as a structure factor and is related to the tortuosity of the pore space; it can be estimated as follows[35]: $\mathcal{G}(\mathbf{x}) = (1/2)[1 + (1/\bar{\phi}(\mathbf{x}))]$.

In order to include the frequency dependency, we follow the approach given in Ref. 3 and Ref. 36. Let $K(\mathbf{x})$, $K_{rn}(S_m)$, $K_{rw}(S_m)$ and $K_{rnw}(S_n)$ denote the absolute and relative permeability functions, respectively and set $\mathcal{A}(\mathbf{x}) = K(\mathbf{x})(K_{rn}K_{rw} - K_{rnw}^2)$, $\mathcal{A}_n(\mathbf{x}) = K_{rw}/\mathcal{A}(\mathbf{x})$, $\mathcal{A}_w(\mathbf{x}) = K_{rn}/\mathcal{A}(\mathbf{x})$. Then we take these coefficients to be of the form:

$$g_l(\mathbf{x}, \omega) = \mathcal{G}\rho_l\bar{S}_l/\bar{\phi} + \mu_l(\bar{S}_l)^2\mathcal{A}_lF_I(\theta_l)/\omega\,, \qquad l = n, w, \tag{2.10}$$

$$g_{nw}(\mathbf{x}, \omega) = \epsilon\mathcal{G}(\rho_n\rho_w\bar{S}_n\bar{S}_w)^{\frac{1}{2}}/\bar{\phi} + (\mu_n\mu_w)^{\frac{1}{2}}\bar{S}_n\bar{S}_wK_{rnw}F_I(\theta_{nw})/(\omega\mathcal{A})\,, \tag{2.11}$$

$$d_l(\mathbf{x}, \omega) = \mu_l(\bar{S}_l)^2\mathcal{A}_lF_R(\theta_l)\,, \qquad l = n, w\,, \tag{2.12}$$

$$d_{nw}(\mathbf{x}, \omega) = (\mu_n\mu_w)^{\frac{1}{2}}\bar{S}_n\bar{S}_wK_{rnw}F_R(\theta_{nw})/\mathcal{A}\,. \tag{2.13}$$

The constants μ_n, μ_w are the fluid viscosities. The coupling permeability term $K_{rnw}(S_n)$ appears when studying quasistatics and dynamics of flow of two immiscible fluids in deformable porous media using homogenization techniques,[37,38] where, for the case of plane slits or cylindrical ducts, explicit expressions for K_{rnw} were obtained. The relative permeability functions must satisfy the relation $K(K_{rn}K_{rw} - K_{rnw}^2) > 0$, such that the two-phase Darcy's law is physically meaningful.

The complex valued frequency dependent function $F(\theta_j) = F_R(\theta_j) + iF_I(\theta_j)$, $j = n, w, nw$ is the frequency correction function defined by Biot[3] in the high-frequency range:

$$F(\theta) = \frac{1}{4}\frac{\theta T(\theta)}{1 - \dfrac{2}{i\theta}T(\theta)}\,, \quad T(\theta) = \frac{\mathrm{ber}'(\theta) + i\mathrm{bei}'(\theta)}{\mathrm{ber}(\theta) + i\mathrm{bei}(\theta)}\,,$$

with $\mathrm{ber}(\theta)$ and $\mathrm{bei}(\theta)$ being the Kelvin functions of the first kind and zero order. The arguments θ_j for $F(\theta_j)$, $j = n, w, nw$ in (2.10)–(2.13) are the generalization for two-phase fluids of the argument given in Refs. 3 and 36 for single-phase fluids:

$$\theta_l = a_p^l\sqrt{\omega\rho_l/\mu_l}\,, \quad a_p^l = a_p^l(\mathbf{x}) = 2\sqrt{K(\mathbf{x})K_{rl}A_0/\bar{\phi}(\mathbf{x})}\,, \quad l = n, w, nw\,, \tag{2.14}$$

where A_0 denotes the Kozeny–Carman constant.[30,39] Taking into account the fact that $F_R(\theta) \to 1$ and $F_I(\theta)/\omega \to 0$ as $\omega \to 0$ we may regard (2.7)–(2.9) as the general form of the equations of motion for frequencies ranging from the seismic to the ultrasonic range.

The plane wave analysis performed in Ref. 15 shows that in these type of media, three different compressional waves (Type I, Type II and Type III) and one shear wave (or S-wave)

can propagate. The Type-I wave is the analogue of the classical fast P-wave propagating in elastic or viscoelastic isotropic solids, while the Type-II and Type-III waves are slow waves strongly attenuated in the low frequency range, corresponding to motions out of phase of the solid and fluid phases. The characteristics of the particle motions of the three phases are analyzed in detail in Sec. 4.

If k^j, $j = I$, II, III, S, denote the complex wavenumbers, the phase velocities c^j and attenuation coefficients α_j (in dB) are given by[12,17]:

$$c^j = \omega/\mathrm{Re}(k^j)\,, \quad \alpha^j = 2\pi 8.685889|Im(k^j)/\mathrm{Re}(k^j)|\,, \quad j = I,\, II,\, III,\, S\,. \tag{2.15}$$

3. The Domain Decomposition Iteration

We consider the solution of Eqs. (2.7)–(2.9) in a two-dimensional poro-viscoelastic bounded domain Ω in the $(x,\, z)$-plane. Let us decompose Ω into a nonoverlapping set of subdomains Ω_j such that $\bar{\Omega} = \cup_{j=1}^{J} \bar{\Omega}_j$ (here $\bar{\Omega} = \Omega \cup \partial\Omega$ denotes the closure of Ω). Set $\Gamma_j = \partial\Omega \cap \partial\Omega_j$ and $\Gamma_{jk} = \partial\Omega_j \cap \partial\Omega_k$, and denote by ξ_j and ξ_{jk} the midpoints of Γ_j and Γ_{jk}, respectively. Also denote by ν_{jk} the unit outer normal on Γ_{jk} from Ω_j to Ω_k and by ν_j the unit outer normal to Γ_j. Then we seek the solution of our differential problem over each subdomain Ω_j as follows: for $j = 1, \ldots, J$, find $u_j(x,\, z,\, \omega) = (u_j^s(x,\, z,\, \omega),\, u_j^n(x,\, z,\, \omega),\, u_j^w(x,\, z,\, \omega))$ such that, for $(x,\, z) \in \Omega_j$,

$$-\omega^2(\rho u_j^s + \rho_n \bar{S}_n u_j^n + \rho_w \bar{S}_w u_j^w) - \nabla \cdot \tau(u_j) = f^s\,, \tag{3.1}$$

$$-\omega^2(\rho_n \bar{S}_n u_j^s + g_n u_j^n + g_{n,w} u_j^w) + i\omega d_n u_j^n - i\omega d_{n,w} u_j^w + \nabla \mathcal{T}_n(u_j) = f^n\,, \tag{3.2}$$

$$-\omega^2(\rho_w \bar{S}_w u_j^s + g_{n,w} u_j^n + g_w u_j^w) + i\omega d_w u_j^w - i\omega d_{n,w} u_j^n + \nabla \mathcal{T}_w(u_j) = f^w\,. \tag{3.3}$$

This differential system needs a set of boundary conditions, taken as follows: at the interior interfaces Γ_{jk} between Ω_j and the neighboring subdomains Ω_k, we have the natural consistency conditions

$$u_j^s = u_k^s\,, \quad u_j^n \cdot \nu_{jk} = -u_k^n \cdot \nu_{kj}\,, \quad u_j^w \cdot \nu_{jk} = -u_k^w \cdot \nu_{kj}\,, \tag{3.4}$$

$$\tau(u_j)\nu_{jk} = -\tau(u_k)\nu_{kj}\,, \quad \mathcal{T}_n(u_j) = \mathcal{T}_n(u_k)\,, \quad \mathcal{T}_w(u_j) = \mathcal{T}_w(u_k)\,, \quad (x,\, z) \in \Gamma_{jk}\,. \tag{3.5}$$

Also, if Ω_j has a part Γ_j of its boundary contained in $\partial\Omega$, we impose the absorbing boundary condition (see Ref. 40)

$$\begin{aligned}&(-\tau(u_j)\nu_j \cdot \nu_j,\, -\tau(u_j)\nu_j \cdot \chi_j,\, \mathcal{T}_n,\, \mathcal{T}_w)\\ &\quad = i\omega\mathcal{B}(u_j^s \cdot \nu_j,\, u_j^s \cdot \chi_j,\, u_j^n \cdot \nu_j,\, u_j^w \cdot \nu_j)\,, \quad (x,\, z) \in \Gamma_j\end{aligned} \tag{3.6}$$

where χ_j is a unit tangent on Γ_j so that $\{\nu_j,\, \chi_j\}$ form an orthonormal system on Γ_j and the symmetric positive definite matrix $\mathcal{B}$ is given by[40]

$$\mathcal{B} = [(\mathcal{M}^{-1}\mathcal{E})^t]^{\frac{1}{2}}\mathcal{M} = \mathcal{M}^{\frac{1}{2}}\mathcal{D}^{\frac{1}{2}}\mathcal{M}^{\frac{1}{2}}\,, \tag{3.7}$$

where $\mathcal{D} = \mathcal{M}^{-\frac{1}{2}}\mathcal{E}\mathcal{M}^{-\frac{1}{2}}$ and

$$\mathcal{M} = \begin{bmatrix} \rho & 0 & \bar{S}_n\rho_n & \bar{S}_w\rho_w \\ 0 & \hat{\rho} & 0 & 0 \\ \bar{S}_n\rho_n & 0 & g_n & g_{nw} \\ \bar{S}_w\rho_w & 0 & g_{nw} & g_w \end{bmatrix}, \quad \mathcal{E} = \begin{bmatrix} K_c^r + N^r & 0 & B_1 & B_2 \\ 0 & N^r & 0 & 0 \\ B_1 & 0 & M_1 & M_3 \\ B_2 & 0 & M_3 & M_2 \end{bmatrix},$$

with

$$\hat{\rho} = \rho - (g_w(\rho_n\bar{S}_n)^2 + g_n(\rho_w\bar{S}_w)^2 - 2g_{nw}\rho_n\bar{S}_n\rho_w\bar{S}_w)/(g_ng_w - g_{nw}^2)\,.$$

In any domain decomposition iteration the objective is to localize the calculations. Thus, let $t = 0, 1, 2, \ldots$ denote the iteration level and let $u_j^t = (u_j^{s,t}, u_j^{n,t}, u_j^{w,t})$ be the solution of (3.1), (3.2), (3.3), (3.4), (3.5) and (3.6) at the t-iteration level, with the variables u_k in the right-hand side of (3.4) and (3.5) replaced by u_k^{t-1} and regarded as data coming from the previous iteration level $t-1$. Furthermore, following the ideas in Refs. 22 and 21, instead of (3.4)–(3.5) we use an equivalent Robin transmission boundary condition, stated for Ω_j in iterative form as follows:

$$\begin{aligned} &(\tau(u_j^t)\nu_{jk}\cdot\nu_{jk},\, \tau(u_j^t)\nu_{jk}\cdot\chi_{jk},\, -\mathcal{T}_n(u_j^t),\, -\mathcal{T}_w(u_j^t)) \\ &\quad + i\omega\beta_{jk}(u_j^{s,t}\cdot\nu_{jk},\, u_j^{s,t}\cdot\chi_{jk},\, u_j^{n,t}\cdot\nu_{jk},\, u_j^{w,t}\cdot\nu_{jk}) \\ &= (\tau(u_k^{t-1})\nu_{kj}\cdot\nu_{kj},\, \tau(u_k^{t-1})\nu_{kj}\cdot\chi_{kj},\, -\mathcal{T}_n(u_k^{t-1}),\, -\mathcal{T}_w(u_k^{t-1})) \\ &\quad - i\omega\beta_{jk}(u_k^{s,t-1}\cdot\nu_{kj},\, u_k^{s,t-1}\cdot\chi_{kj},\, u_k^{n}\cdot\nu_{kj},\, u_k^{w,t-1}\cdot\nu_{kj})\,, \quad (x,\, z)\in\Gamma_{jk}\subset\partial\Omega_j\,. \end{aligned} \tag{3.8}$$

Here β_{jk} is a positive definite matrix function defined on the interior boundaries Γ_{jk} and χ_{jk} is a unit tangent on Γ_{jk} so that $\{\nu_{jk}, \chi_{jk}\}$ form an orthonormal system on Γ_{jk}. For the neighboring subdomains Ω_k we impose a boundary condition similar to (3.8) exchanging the roles of u_j^t and u_k^{t-1} and with *the same parameter* β_{jk}.[22,21]

First, we define the domain decomposed iterative procedure for the case in which the domain decomposition partition coincides with the finite element partition $\mathcal{N}^h$ of Ω into rectangles Ω_j of diameter bounded by h. The changes needed in the procedure to treat the case of larger subdomains are indicated at the end of the section.

To approximate each component of the solid displacement vector u_j^s in each Ω_j, take a reference rectangle $\hat{R} = [-1,\, 1]^2$ and consider the nonconforming finite element space $\mathcal{V}(\hat{R})$ constructed as in Ref. 26: the local degrees of freedom will be the values of each component of u_j^s at the mid points $\xi^L = (-1,\, 0)$, $\xi^B = (0,\, -1)$, $\xi^R = (1,\, 0)$ and $\xi^T = (0,\, 1)$ of the sides of $\hat{R}$. Thus set $\varsigma(x) = x^2 - (5/3)x^4$ and choose the following local finite element basis:

$$\begin{aligned} \varphi^L(x,\, z) &= \frac{1}{4} - \frac{1}{2}x - \frac{3}{8}(\varsigma(x) - \varsigma(z))\,, \quad \varphi^R(x,\, z) = \frac{1}{4} + \frac{1}{2}x - \frac{3}{8}(\varsigma(x) - \varsigma(z))\,, \\ \varphi^B(x,\, z) &= \frac{1}{4} - \frac{1}{2}z + \frac{3}{8}(\varsigma(x) - \varsigma(z))\,, \quad \varphi^T(x,\, z) = \frac{1}{4} + \frac{1}{2}z + \frac{3}{8}(\varsigma(x) - \varsigma(z))\,. \end{aligned} \tag{3.9}$$

Then we define $\mathcal{V}(\hat{R}) = \mathrm{Span}\{\varphi^L,\, \varphi^R,\, \varphi^B,\, \varphi^T\}$.

To approximate the fluid displacement vectors u_j^n and u_j^w, we choose the vector part of the Raviart–Thomas–Nedelec space[27,28] of zero order defined on $\hat{R}$ as follows. The four degrees of freedom associated with each fluid displacement vector are the values of the normal components at the mid points ξ^l, $l = L, R, B, T$ of the faces of $\hat{R}$. Thus, defining the local basis $\psi^L(x) = -1 + x$, $\psi^R(x) = x$, $\psi^B(z) = -1 + z$, $\psi^T(z) = z$, we have that $\mathcal{W}(\hat{R}) = \text{Span}\{(\psi^L(x), 0), (\psi^R(x), 0), (0, \psi^B(z)), (0, \psi^T(z))\}$.

Now, our finite element approximations U^l to u^l, $l = n, w$ and $U^s = (U_1^s, U_2^s)$ to $u^s = (u_1^s, u_2^s)$ in the reference element $\hat{R}$ are represented as follows:

$$\begin{aligned} U^l &= U^{l,L}(\psi^L(x), 0) + U^{l,R}(\psi^R(x), 0) + U^{l,B}(0, \psi^B(z)) + U^{l,T}(0, \psi^T(z)), \quad l = n, w\,, \\ U_m^s &= U_m^{s,L}\varphi^L(x, z) + U_m^{s,B}\varphi^B(x, z) + U_m^{s,R}\varphi^R(x, z) + U_m^{s,T}\varphi^T(x, z), \quad m = 1, 2\,, \end{aligned} \tag{3.10}$$

By properly scaling the given basis elements we construct the spaces $\mathcal{V}_j^h = \mathcal{V}(\Omega_j)$ and $\mathcal{W}_j^h = \mathcal{W}(\Omega_j)$ used to represent in (3.10) the approximating functions U_j^s, U_j^n and U_j^w for the solid and fluid displacement vectors on each element Ω_j.

Following Refs. 26, 22 and 21, for computational convenience, we consider a hybridized form of the above formulation by introducing a set of Lagrange multipliers $\eta_{jk} = (\eta_{jk}^{s,\nu}, \eta_{jk}^{s,\chi}, \eta_{jk}^n, \eta_{jk}^w)$ associated with the values of the generalized forces at the mid points ξ_{jk} of Γ_{jk} in the following sense: $\eta_{jk}^{s,\nu} \sim (\tau(U_j)\nu_{jk} \cdot \nu_{jk})(\xi_{jk})$, $\eta_{jk}^{s,\chi} \sim (\tau(U_j)\nu_{jk} \cdot \chi_{jk})(\xi_{jk})$, $\eta_{jk}^n \sim \mathcal{T}_n(U_j)(\xi_{jk})$, $\eta_{jk}^w \sim \mathcal{T}_w(U_j)(\xi_{jk})$. The Lagrange multipliers belong to the space of functions defined as follows: $\Lambda^h = \{\eta : \eta|_{\Gamma_{jk}} = \eta_{jk} \in [P_0(\Gamma_{jk})]^4 = \Lambda_{jk}^h, \forall\{j, k\}\}$, where $P_0(\Gamma_{jk})$ denotes the constant functions on Γ_{jk}.

Next, we state a domain decomposition iteration using a variational formulation. For $t = 0, 1, 2, \ldots$, let $U_j^t = (U_j^{s,t}, U_j^{n,t}, U_j^{w,t})$ and η_{jk}^t be the discrete displacement vectors and the Lagrange multipliers at the t-iteration level. Let us denote by $(\cdot, \cdot)_j$ the usual complex inner product in $L^2(\Omega_j)$. Moreover, for $\Gamma = \Gamma_j$ or $\Gamma = \Gamma_{jk}$ let $\langle \cdot, \cdot \rangle_\Gamma$ denote the complex inner product in $L^2(\Gamma)$, and let $\langle\langle u, v \rangle\rangle_\Gamma$ denote its approximation by the mid-point quadrature: $\langle\langle u, v \rangle\rangle_\Gamma = (u\overline{v})(\xi_{jk})|\Gamma|$ where $|\Gamma|$ is the measure of Γ.

Then, with $U_j^t = (U_j^{s,t}, U_j^{n,t}, U_j^{w,t})$ replacing u_j in (3.1)–(3.3), (3.6) and (3.8), and $U_k^{t-1} = (U_k^{s,t-1}, U_k^{n,t-1}, U_k^{w,t-1})$ replacing u_k in (3.8), multiply (3.1), (3.2) and (3.3) by $v^s \in [\mathcal{V}_j^h]^2$, $v^n \in \mathcal{W}_j^h$ and $v^w \in \mathcal{W}_j^h$, respectively, and integrate over Ω_j, using integration by parts in the terms $(\nabla \cdot \tau(U_j^t), v^s)_j$, $(\nabla \mathcal{T}_n(U_j^t), v^n)_j$ and $(\nabla \mathcal{T}_w(U_j^t), v^w)_j$. Then apply the boundary conditions (3.6) and (3.8) and approximate the boundary integrals on Γ_j and Γ_{jk} using the mid-point quadrature rule, using the identification of the generalized forces at the mid points ξ_{jk} with the Lagrange multipliers η_{jk}. Adding the resulting equations, we see that the domain decomposition iteration can be stated as follows: given $(U_j^0, \eta_{jk}^0) \in [\mathcal{V}_j^h]^2 \times \mathcal{W}_j^h \times \mathcal{W}_j^h \times \Lambda_{jk}^h$ for all j, for $t = 1, 2, 3, \ldots$, find $(U_j^t, \eta_{jk}^t) \in [\mathcal{V}_j^h]^2 \times \mathcal{W}_j^h \times \mathcal{W}_j^h \times \Lambda_{jk}^h$ such that

$$\begin{aligned} &-\omega^2(\rho U_j^{s,t} + \rho_n \bar{S}_n U_j^{n,t} + \rho_w \bar{S}_w U_j^{w,t}, v^s)_j - \omega^2(\rho_n \bar{S}_n U_j^{s,t} + g_n U_j^{n,t} + g_{n,w} U_j^{w,t}, v^n)_j \\ &\quad - \omega^2(\rho_w \bar{S}_w U_j^{s,t} + g_{n,w} U_j^{n,t} + g_w U_j^{w,t}, v^w)_j + i\omega(d_n U_j^{n,t}, v^n)_j \end{aligned}$$

$$
\begin{aligned}
&- i\omega(d_{n,w}U_j^{w,t},\, v^n)_j + i\omega(d_w U_j^{w,t},\, v^w)_j - i\omega(d_{n,w}U_j^{n,t},\, v^w)_j \\
&+ \sum_{pq}(\tau_{pq}(U_j^t),\, \varepsilon_{pq}(v^s))_j - (\mathcal{T}_n(U_j^t),\, \nabla\cdot v^n)_j - (\mathcal{T}_w(U_j^t),\, \nabla\cdot v^w)_j \\
&+ \langle\langle i\omega\mathcal{B}(U_j^{s,t}\cdot\nu_j,\, U_j^{s,t}\cdot\chi_j,\, U_j^{n,t}\cdot\nu_j,\, U_j^{w,t}\cdot\nu_j),\, (v^s\cdot\nu_j,\, v^s\cdot\chi_j,\, v^n\cdot\nu_j,\, v^w\cdot\nu_j)\rangle\rangle_{\Gamma_j} \\
&+ \sum_k \langle\langle i\omega\beta_{jk}(U_j^{s,t}\cdot\nu_{jk},\, U_j^{s,t}\cdot\chi_{jk},\, U_j^{n,t}\cdot\nu_{jk}, \\
&U_j^{w,t}\cdot\nu_{jk}),\, (v^s\cdot\nu_{jk},\, v^s\cdot\chi_{jk},\, v^n\cdot\nu_{jk},\, v^w\cdot\nu_{jk})\rangle\rangle_{\Gamma_{jk}} \\
&= (f^s,\, v^s)_j + (f^n,\, v^n)_j + (f^w,\, v^w)_j \\
&- \sum_k \langle\langle i\omega\beta_{jk}(U_k^{s,t-1}\cdot\nu_{kj},\, U_k^{s,t-1}\cdot\chi_{kj},\, U_k^{n,t-1}\cdot\nu_{kj},\, U_k^{w,t-1}\cdot\nu_{kj}), \\
&(v^s\cdot\nu_{jk},\, v^s\cdot\chi_{jk},\, v^n\cdot\nu_{jk},\, v^w\cdot\nu_{jk})\rangle\rangle_{\Gamma_{jk}}, \\
&- \sum_k \langle\langle(-\eta_{kj}^{s,\nu,t-1},\, -\eta_{kj}^{s,\chi,t-1},\, \eta_{kj}^{n,t-1},\, \eta_{kj}^{w,t-1}),\, (v^s\cdot\nu_{jk},\, v^s\cdot\chi_{jk},\, v^n\cdot\nu_{jk},\, v^w\cdot\nu_{jk})\rangle\rangle_{\Gamma_{jk}}, \\
&\qquad\qquad (v^s,\, v^n,\, v^w)\in[\mathcal{V}_j^h]^2\times\mathcal{W}_j^h\times\mathcal{W}_j^h\times\Lambda_{jk}^h\,, \qquad (3.11)
\end{aligned}
$$

$$
\begin{aligned}
&(\eta_{jk}^{s,\nu,t},\, \eta_{jk}^{s,\chi,t},\, -\eta_{jk}^{n,t},\, -\eta_{jk}^{w,t}) \\
&\quad = (\eta_{kj}^{s,\nu,t-1},\, \eta_{kj}^{s,\chi,t-1},\, -\eta_{kj}^{n,t-1},\, -\eta_{kj}^{w,t-1}) - i\omega\beta_{jk}(U_j^{s,t}\cdot\nu_{jk} + U_k^{s,t-1}\cdot\nu_{kj}, \\
&\qquad U_j^{s,t}\cdot\chi_{jk} + U_k^{s,t-1}\cdot\chi_{kj},\, U_j^{n,t}\cdot\nu_{jk} + u_k^{n,t-1}\cdot\nu_{kj},\, U_j^{w,t}\cdot\nu_{jk} + U_k^{w,t-1}\cdot\nu_{kj})(\xi_{jk})\,. \qquad (3.12)
\end{aligned}
$$

Equation (3.12), used to update the Lagrange multipliers, is obtained directly from (3.8) evaluated at the mid point ξ_{jk}. Equation (3.11) yields a 16×16 linear system of equations for the degrees of freedom associated with the vector displacements of the three phases on each subdomain Ω_j at the t-iteration level. After solving these systems, the Lagrange multipliers are updated using (3.12). The iteration (3.11)–(3.12) is a Jacobi-type iteration. A twice as fast iteration may also be defined by using a **red–black** type iteration (see Refs. 22 and 21).

The arguments given in Refs. 22 and 21 can be used here to show that the iteration (3.11)–(3.12) converges and it is first order correct in the spatial discretization. The iteration parameter matrix β_{jk} is chosen to have the same form of the matrix $\mathcal{B}$ in (3.6). The space-time solution is obtained by solving (3.11)–(3.12) for a finite number of frequencies and an approximate inverse Fourier transform. See Ref. 20 for an analysis of this procedure.

Finally, let us indicate the changes needed to treat the case of larger subdomains Ω_j. For simplicity let us assume that the finite element partition $\mathcal{N}_j^h$ associated with each subdomain Ω_j is a subset of the global finite element partition $\mathcal{N}^h$ of Ω into rectangles of size bounded by h. Let $\bar\Omega_j = \cup_{l=1}^{L_j}\bar R_j^l$ be a partition on each Ω_j into rectangles R_j^l and denote by ξ_{lm}^j

the midpoint of the common interface between the adjacent rectangles R_j^l and R_j^m. The nonconforming finite element space $\mathcal{V}_j^h$ used to approximate each component of the solid displacement vector and the space $\mathcal{W}_j^h$ used to approximate each fluid displacement vector are: $\mathcal{V}_j^h = \{v \in L^2(\Omega_j) : v_l^j = v|_{R_j^l} \in \mathcal{V}(R_j^l),\ l = 1, \ldots, L_j;\ v_l^j(\xi_{lm}^j) = v_m^j(\xi_{lm}^j),\ \forall\{l, m\}\}$ and $\mathcal{W}_j^h = \{v \in H(\mathrm{div}, \Omega_j) : v_l^j = v|_{R_j^l} \in W(R_j^l),\ l = 1, \ldots, L_j\}$ where $H(\mathrm{div}, \Omega_j) = \{v \in [L^2(\Omega_j)]^2 : \nabla \cdot v \in L^2(\Omega_j)\}$. Finally, let us write each common interface Γ_{jk} between two adjacent subdomains Ω_j and Ω_k as follows: $\Gamma_{jk} = \bigcup_{l,m} \gamma_{jk}^{l,m}$, where $\gamma_{jk}^{l,m}$ denotes any of the common sides of rectangles R_j^l and R_k^m in the partitions $\mathcal{T}_j^h$ and $\mathcal{T}_k^h$ such that $\gamma_{jk}^{l,m} \subset \Gamma_{jk}$. Then, we define $\Lambda^h = \{\eta : \eta|_{\Gamma_{jk}} = \eta_{jk} \in \Pi_{l,m}\ [P_0(\gamma_{jk}^{l,m})]^4 = \Lambda_{jk}^h,\ \forall\{j, k\}\}$.

With this new definitions of the spaces $\mathcal{V}_j^h$, $\mathcal{W}_j^h$ and Λ^h, the definition of the iterative procedure in (3.11)–(3.12) remains unchanged.

4. Numerical Experiments

We use the iterative procedure (3.11)–(3.12) to simulate the propagation of waves in a sample of Nivelsteiner sandstone, a friable sandstone mainly composed of quartz with small percentages of rock fragments and potash-feldspar.[29] Its material properties, taken from Ref. 8, are $\phi = 0.33$, $K = 5000$ mD, $\rho_s = 2.65$ gr/cm^3, grain bulk modulus $K_s = 36$ GPa, frame bulk modulus $K_m = 6.21$ GPa and frame shear modulus, $N = 4.55$ GPa. The pore space is assumed to be filled by 90% water (as the wetting phase) and 10% of hydrocarbon gas. Their properties are: $\rho_w = 1\,\mathrm{gr/cm^3}$, $\mu_w = 0.01\,\mathrm{Poise}$, $K_w = 2.223$ GPa, $\rho_n = 0.1$ gr/cm^3, $\mu_n = 0.00015$ Poise, $K_n = 0.022$ GPa. The reference fluid pressure $\bar{P}_w$ is taken 30 MPa, corresponding to the hydrostatic pressure at a burial depth of about 3 Km.

The relative permeability functions $K_{rn}(S_n)$ and $K_{rw}(S_n)$ and the capillary pressure function $P_{ca}(S_n)$ and needed to describe our system are taken to be[41]:

$$K_{rn}(S_n) = (1 - (1 - S_n)/(1 - S_{rn}))^2\,, \quad K_{rw}(S_n) = ([1 - S_n - S_{rw}]/(1 - S_{rw}))^2\,,$$
$$P_{ca}(S_n) = A(1/(S_n + S_{rw} - 1)^2 - S_{rn}^2/[S_n(1 - S_{rn} - S_{rw})]^2)\,. \tag{4.1}$$

These relations are based on laboratory experiments performed on different porous rocks during imbibition and drainage processes (neglecting hysteresis effects). In the numerical experiment, we chose $S_{rw} = S_{rn} = 0.05$, and $A = 30$ kPa. The resulting capillary pressure at $\bar{S}_n = 0.1$ is about 3.4 kPa. In the absence of proper experimental data, the coupling permeability function $K_{rnw}(S_n)$ used in this work is assumed to be $K_{rnw}(S_n) = \sqrt{\epsilon K_{rn}(S_n) K_{rw}(S_n)}$. The parameter ϵ in (2.11) and the equation above is equal to 0.1, as in Ref. 15.

The viscoelastic parameters describing the dissipative behavior of the saturated sandstone are $\hat{Q}_l = 30$, 20, for $l = K_c$, N, respectively, $T_{1,l} = 10$ ms^{-1}, $T_{1,l} = 10^9$ ms^{-1}, for $l = K_c$, N.

According to the equations given in Sec. 2, the three characteristic frequencies at this saturation state are approximately $\omega_c^n = 197$ kHz, $\omega_c^w = 41$ kHz and $\omega_c^{nw} = 83$ kHz. The values of the phase velocities and attenuation coefficients at the central frequency $f_0 = 500$ kHz

Table 1. Phase velocities and attenuation factors at 500 kHz for gas saturation 10%.

	Poro-elastic		Poro-viscoelastic	
Wave	c^j (Km/s)	α^j (db)	c^j (Km/s)	α^j (db)
Type I P	2.54540280	0.10571459	2.52993880	1.2232244
Type II P	0.27500635	1.36782290	0.27498727	1.3839098
Type III P	0.41792553	2.48654420	0.41790992	2.4968665
Shear	1.53234320	0.12485457	1.52128970	1.4605364

are given in Table 1 for $\bar{S}_n = 0.1$. We compare the values corresponding to the poroelastic and the poro-viscoelastic formulations. The computations include poro-viscoelasticity and frequency dependent mass coupling and viscous drag coefficients, as described in Secs. 2.2 and 2.3. The value of the Kozeny–Carman constant A_0 in (2.14) is equal to 5.[39]

Figures 1 and 2 show the phase velocities and attenuation coefficients for the three compressional waves and the shear wave versus nonwetting saturation, at the central frequency of the source. Notice in Fig. 2(b) the change in behavior of the attenuation coefficients of the two slow modes, indicating that for high nonwetting saturation values only the new Type-III wave can be observed.

In the following numerical experiments, we show snapshots and traces of the particle velocity fields in the solid, the free-gas and the water phase. Our aim is to simulate a laboratory experiment of generation and propagation of body waves at ultrasonic frequencies.

The domain for the 2D numerical simulation is a square of side length 6 cm with a uniform partition $\mathcal{N}^h$ of Ω into squares of side length $h = 1/N_x$, with $N_x = N_z = 640$.

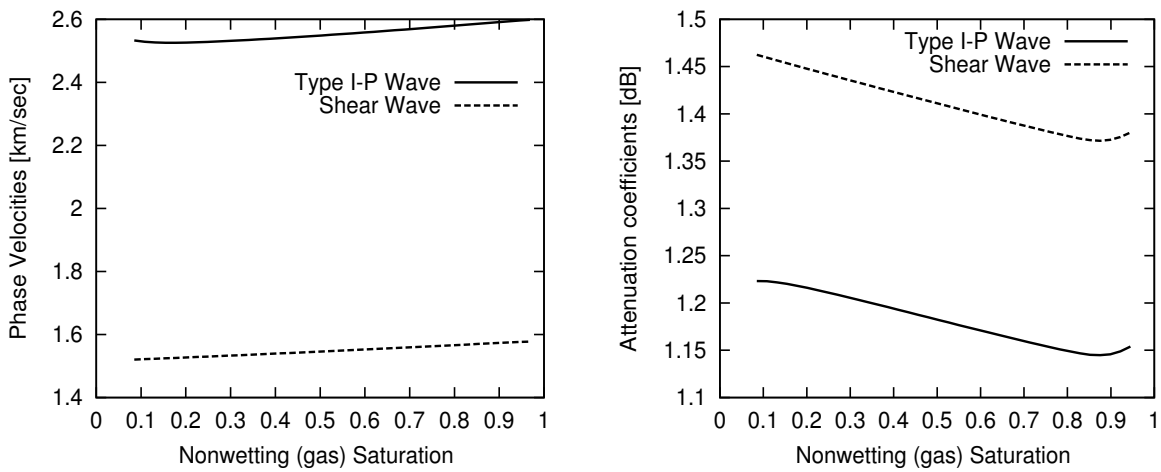

(a) (b)

Fig. 1. Behavior of the Type-I P and shear waves versus nonwetting saturation at the central frequency $\omega = 500$ kHz; (a) phase velocities; (b) attenuation coefficients.

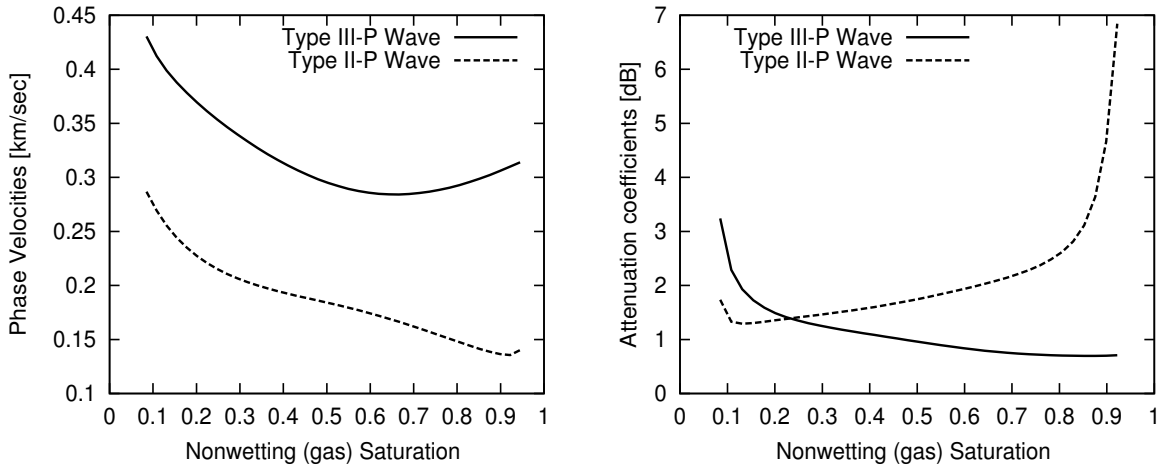

(a) (b)

Fig. 2. Behavior of the Type-II and Type-III P-waves versus nonwetting saturation at the central frequency $\omega = 500$ kHz; (a) phase velocities; (b) attenuation coefficients.

The source function $(f^s,\, f^n,\, f^w)$ is a point source located at $(x_s,\, y_s) = (3$ cm, 3 cm) and applied to the solid matrix (dilatational and shear perturbations), and to the fluid phases (dilatational perturbations). More specifically, if δ_{x_s,z_s} denotes the Dirac distribution at $(x_s,\, y_s)$, and we define the distribution $\epsilon_{12}\delta_{x_s,z_s}$ by the rule $\epsilon_{12}\delta_{x_s,z_s} = (\partial\delta_{x_s,z_s}/\partial z,\, \partial\delta_{x_s,z_s}/\partial x)$, then

$$f^s(x,\, z,\, \omega) = \nabla\delta_{x_s,z_s} g(\omega) + 2\epsilon_{12}\delta_{x_s,z_s} g(\omega)\,,$$
$$f^n(x,\, z,\, \omega) = f^w(x,\, z,\, \omega) = \nabla\delta_{x_s,z_s} g(\omega)\,.$$

Here, $g(\omega)$ is the Fourier transform of the waveform $g(t) = -2\xi(t - t_0)e^{-\xi(t-t_0)^2}$, with $f_0 = 500$ kHz denoting the source central (dominant) frequency and $\xi = 8\, f_0^2$, $t_0 = 1.25/f_0$.

The spectrum of $g(\omega)$ is negligible for frequencies ω above $\omega^* = 2\pi$ 1000 kHz. Thus, the iterative procedure (3.11)–(3.12) is used to compute $U^s(x,\, z,\, \omega)$, $U^n(x,\, z,\, \omega)$, $U^w(x,\, z,\, \omega)$ at 90 temporal frequencies ω_m in the interval $(0,\, \omega^*)$ with $\omega_m = m\Delta\omega$ and $\Delta\omega = \omega^*/90$. The solution $U^s(x,\, z,\, t)$, $U^n(x,\, z,\, t)$, $U^w(x,\, z,\, t)$ at the discrete times $t = t_l = l\Delta t$, $l = 1,\, 2, \ldots,\, L$, is obtained by using the discrete time Fourier transform. Here, $L = T/\Delta t$ and T is the maximum simulation time, equal to 0.08 ms in all the experiments. We emphasize that the choice of the time step Δt is not restricted by any Courant–Friedrichs–Lewy stability condition as in explicit algorithms formulated in the space-time domain. In fact, for any time t_l we truncate the integral in the inverse Fourier transform for $\omega > \omega^*$ and compute the truncated integral using the mid-point quadrature rule. The error introduced by this approximation is proportional to $(h + (\Delta\omega)^2)$ (see Ref. 20).

Figure 3 shows snapshots of the vertical component of the particle velocity at $t = 0.018$ ms for the solid skeleton and the vertical components of the relative particle velocity of the nonwetting and wetting phases, denoted by $V^s(x,\, z,\, t)$, $V^n(x,\, z,\, t)$ and $V^w(x,\, z,\, t)$,

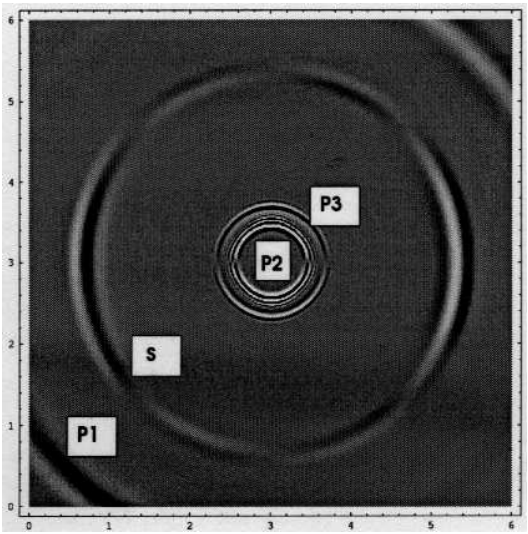

(a)

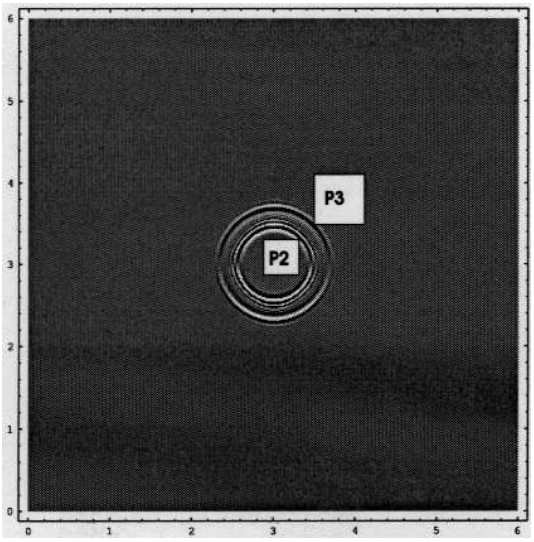

(b)

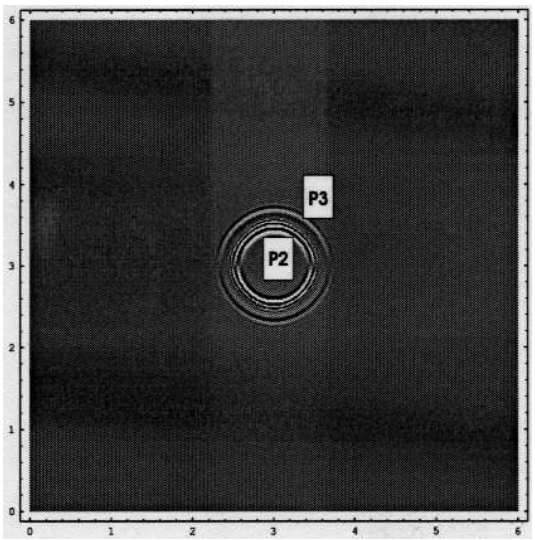

(c)

Fig. 3. Snapshots of the vertical particle velocity at $t = 0.018$ ms. The snapshots correspond to the (a) solid skeleton; (b) gas phase and (c) water phase. The relative amplitude relation between the snapshots is 1/211/30, respectively.

respectively. The relative amplitude relation between the snapshots in Figs. 3, 4 and 5 is 1/211/30, which indicates that the two slow modes are much stronger in the fluid phases. In the solid phase, we observe four wavefronts, associated with the fast P-wave, the S-wave and the two slow waves, labeled P1, S, P2 and P3. The Type I-wave front is hitting the

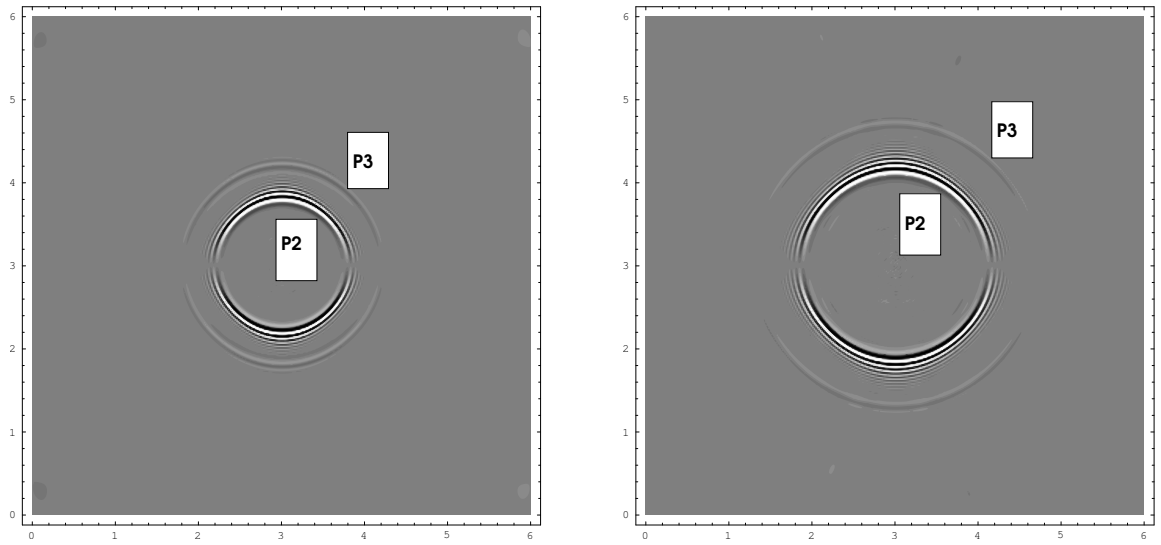

(a) (b)

Fig. 4. Snapshot of the vertical component of the particle velocity of the solid phase at (a) $t = 0.03$ ms and (b) $t = 0.42$ ms.

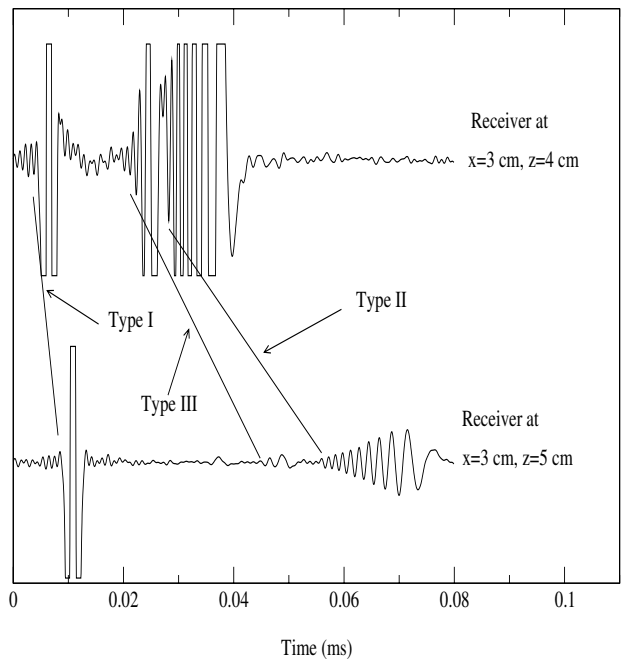

Fig. 5. Trace of the vertical component of the particle velocity of the solid phase V_z^s at two receivers located at $x = 3$ cm, $z = 4$ cm and $x = 3$ cm, $z = 5$ cm.

boundary and leaving the domain without generating artificial reflections, indicating that the absorbing boundary condition (3.6) is performing quite well for simulation purposes.

Figure 4 shows snapshots of the vertical component of the particle velocity of the solid phase at (a) $t = 0.03$ ms and (b) $t = 0.042$ ms, respectively. Since at the latter time, the Type-I and S-wavefronts left the domain, only the two wavefronts associated with the Type-II and Type-III compressional modes can be observed. Notice that the wavefront associated with the fastest of the two slow waves, i.e. the Type-III wave, is much more attenuated compared to the Type-II wavefront. This effect is more noticeable in the snapshot at $t = 0.042$ msec. The snapshots for the nonwetting and wetting phases look quite similar to those of the solid-phase in Fig. 4 and for brevity we do not include them here.

The attenuation curves in Fig. 2(b) show that for nonwetting saturation values above 0.23, we have the opposite situation, i.e. the fastest Type-III wavefront is less attenuated than the Type-II wavefront. This effect was observed numerically.

In order to observe this decay effect in the two slow wavefronts, Fig. 5 displays traces of the vertical component of the particle-velocity of the solid phase at two receivers located at $x = 3$ cm, $z = 4$ cm and $x = 3$ cm, $z = 5$ cm, respectively. The amplitudes are normalized to the maximum value of the trace at the receiver located at $x = 3$ cm, $z = 4$, and then both traces are clipped with the same maximum cutoff to better observe the arrivals of the different waves. It can be seen that the Type-III arrival at the receiver at $x = 3$ cm, $z = 5$ cm is more attenuated than the Type-II arrival in the same receiver.

Figure 6 shows a trace of the vertical component of the total particle velocity $V_z^{s,T} = V_z^s + \bar{S}_n V^n + \bar{S}_w V^w$ at a receiver located at $x = 4$ cm, $z = 3.5$ cm, with normalized amplitude, where the four arrivals associated with the four different modes can clearly be observed.

Figures 7, 8 and 9 are essential to understand the motion of the three phases corresponding to the two slow modes. These figures show traces of the divergence of the solid and the absolute nonwetting and wetting particle velocities $\tilde{V}_z^l = (1/\phi)V_z^l + V_z^s$, $l = n, w$ at the receiver location $x = 4$ cm, $z = 3.5$ cm in the following manner. Figures 7 and 8 show the solid phase versus the nonwetting and wetting phases, respectively, where the traces are first normalized to the maximum value of the corresponding fluid phases, and then, the solid-phase trace is scaled by factors of 282 and 40. Similarly, Fig. 9 shows the wetting and nonwetting fluid divergences, where first both traces are normalized to the maximum value of the nonwetting phase, and then, the wetting-phase trace is scaled by a factor of 3.5. The scaling in Figs. 7, 8 and 9 is used to better observe the particle motion in the two slow modes. After analyzing Figs. 7, 8 and 9, we conclude the following:

1) For the slower of the two slow compressional waves, the solid moves in opposite phase with both fluid phases and the two fluid phases move in phase. Thus, this Type II wave is the analogue of the slow P-wave for single-phase fluids.
2) With regard to the faster of the two slow compressional waves, referred to as Type-III wave, the solid moves in phase with the nonwetting phase and in opposite phase with the wetting phase, and the two fluid phases move in opposite phase. This is a new mode absent in rocks saturated by single-phase fluids.

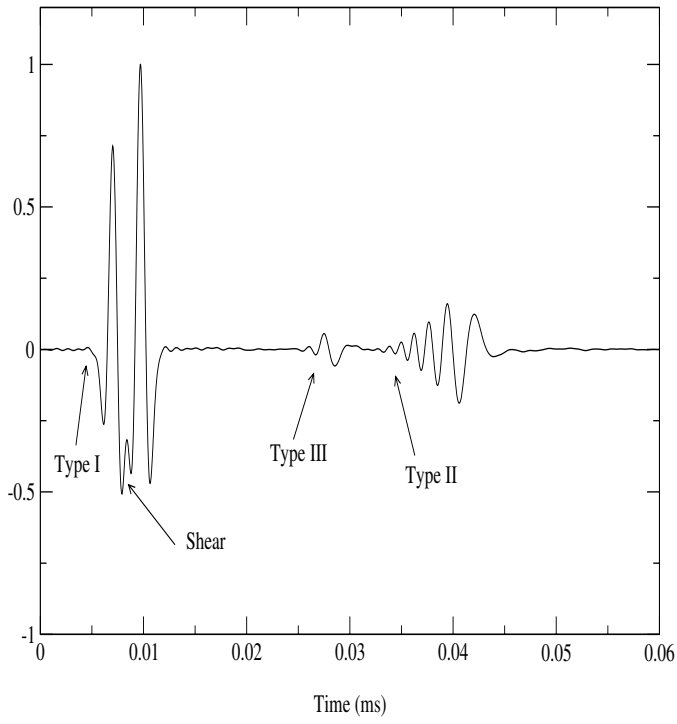

Fig. 6. Trace of the vertical component of the total particle velocity $V_z^T = V_z^s + S_n V^n + S_w V^w$ at a receiver located at $x = 4$ cm, $z = 3.5$ cm. The amplitudes are normalized.

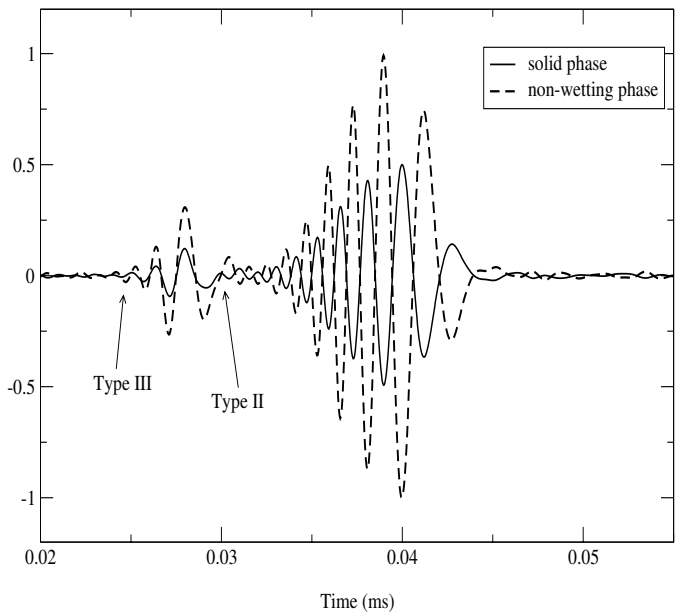

Fig. 7. Traces of the divergence of the particle velocity of the solid and nonwetting fluid phases at a receiver located at $x = 4$ cm, $z = 3.5$ cm.

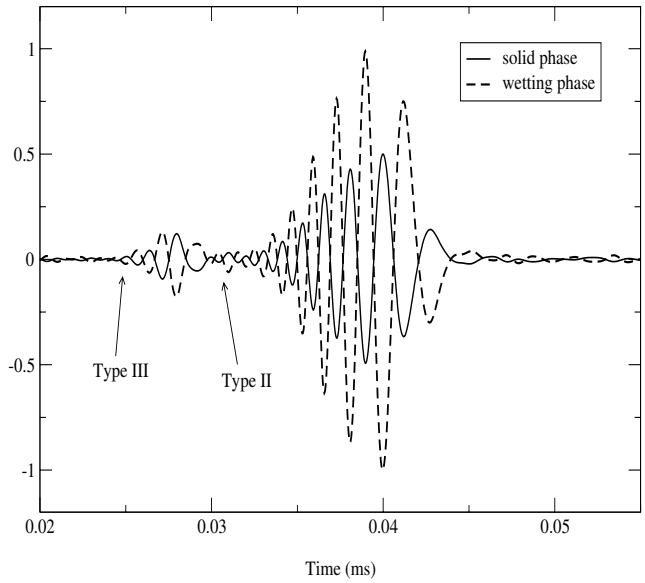

Fig. 8. Traces of the divergence of the particle velocity of the solid and wetting fluid phases at a receiver located at $x = 4$ cm, $z = 3.5$ cm.

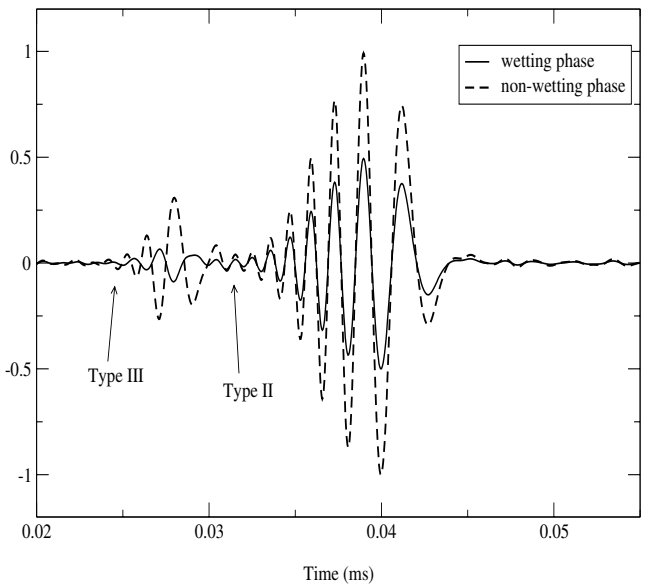

Fig. 9. Traces of the divergence of the particle velocity of the wetting and nonwetting fluid phases at a receiver located at $x = 4$ cm, $z = 3.5$ cm.

5. Conclusions

We have presented a model to describe wave propagation in a poro-viscoelastic medium saturated with a two-phase fluid. The model includes capillary forces and mass and viscous

coupling coefficients in the equations of motion, as well as frequency dependent correction factors in the high-frequency range. We also developed a domain decomposition iteration that allow us to compute approximate solutions. This new procedure is formulated in the space-frequency domain, allowing for the simultaneous and independent solution of the equations at a finite number of frequencies. The space-time solution is obtained by using an inverse Fourier transform. The algorithm is first-order accurate in the spatial discretization and does not require any smoothness assumption or small variability on the coefficients of the differential model. Under the assumption that the model accurately describes the physics involved, a second slow mode (referred to as Type III) has been observed for the first time. This result constitutes a significant departure from the single-phase fluid case. The experiments use a clay-free sandstone saturated with gas and water, a reference fluid pressure $\bar{P}_w = 30$ MPa and gas saturation of 10%, corresponding to a capillary pressure value of 3.4 kPa. At these conditions, the Type-III wave at 500 kHz has a phase velocity of 418 m/s.

The detection and analysis of this new wave mode in real situations may provide information about the nature, saturation and pressure regime of the saturant fluids. Future research involves the use of the numerical simulator to determine the conditions under which the new wave can be detected in laboratory experiments and the analysis of these waves in partially-saturated zones within hydrocarbon reservoirs.

Acknowledgments

This work was funded in part by CONICET, Argentina (PIP 0363/98).

References

1. M. A. Biot, Theory of deformation of a porous viscoelastic anisotropic solid, *J. Appl. Phys.* **27** (1956) 459.
2. M. A. Biot, Theory of propagation of elastic waves in a fluid-saturated porous solid. I. Low frequency range, *J. Acoust. Soc. Am.* **28** (1956) 168.
3. M. A. Biot, Theory of propagation of elastic waves in a fluid-saturated porous solid. II. High frequency range, *J. Acoust. Soc. Am.* **28** (1956) 179.
4. T. J. Plona, Observation of a second bulk compressional wave in a porous medium at ultrasonic frequencies, *Appl. Phys. Lett.* **56** (1980) 259.
5. J. Douglas Jr., J. E. Santos and J. L. Hensley, Simulation of Biot waves in a cylindrically symmetric domain, in *Proc. 3rd Int. Conf. Hyperbolic Problems*, eds. B. Engquist and B. Gustafson (Chartwell-Bratt, **1**, 1990), pp. 330–350.
6. J. L. Hensley, J. Douglas Jr. and J. E. Santos, Dispersion of Type II Biot waves in inhomogeneous media, in *Proc. 6th Int. Conf. Math. Methods in Eng.* (Czechoslovakia, 1991), pp. 67–83.
7. J. Douglas Jr., J. E. Santos, J. L. Hensley and M. E. Morley, Simulation of waves arising in acoustic well-logging, *Rend. Sem. Mat. Univ. Pol. Torino, Fascicolo Speciale, Numerical Methods, 1991*, pp. 223–243.
8. B. Arntsen and J. M. Carcione, Numerical simulation of the Biot slow wave in water-saturated Nivelsteiner sandstone, *Geophysics* **66** (2001) 890.
9. J. M. Carcione and G. Quiroga-Goode, Some aspects of the physics and numerical modeling of Biot compressional waves, *J. Comput. Acoust.* **3** (1996) 261.

10. M. A. Biot, Mechanics of deformation and acoustic propagation in porous media, *J. Appl. Phys.* **33** (1962) 1482.
11. J. Berryman, L. Thigpen and R. Chin, Bulk elastic wave propagation in partially saturated porous solids, *J. Acoust. Soc. Am.* **84** (1988) 360.
12. N. C. Dutta and H. Odé, Attenuation and dispersion of compressional waves in fluid-filled porous rocks with partial gas saturation (White model) – Part I: Biot theory, *Geophysics* **44** (1979) 777.
13. S. Mochizuki, Attenuation in partially saturated rocks, *J. Geophys. Res.* **87** (1982) 8598.
14. M. N. Toksöz, C. H. Cheng and A. Timur, Velocities of seismic waves in porous rocks, *Geophysics* **41** (1976) 621.
15. J. E. Santos, J. Douglas Jr., J. M. Corberó and O. M. Lovera, A model for wave propagation in a porous medium saturated by a two-phase fluid, *J. Acoust. Soc. Am.* **87** (1990a) 1439.
16. J. E. Santos, J. Douglas Jr. and J. Corberó, Static and dynamic behaviour of a porous solid saturated by a two-phase fluid, *J. Acoust. Soc. Am.* **87** (1990b) 1428.
17. J. M. Carcione, *Wave Fields in Real Media: Wave Propagation in Anisotropic, Anelastic and Porous Media* (Pergamon Press, Amsterdam, 2001).
18. J. M. Carcione, Constitutive model and wave equations for linear, viscoelastic, anisotropic media, *Geophysics* **60** (1995) 537.
19. J. Douglas Jr., J. E. Santos and D. Sheen, Approximation of scalar waves in the space-frequency domain, *Math. Models Methods Appl. Sci.* **4** (1994) 509.
20. J. Douglas Jr., J. E. Santos, D. Sheen and L. Bennethum, Frequency domain treatment of one-dimensional scalar waves, *Math. Models Methods Appl. Sci.* **3** (1993) 171.
21. T. Ha, J. E. Santos and D. Sheen, Nonconforming finite element methods for the simulation of waves in viscoelastic solids, *Comp. Methods in Appl. Mech. Eng.* **191** (2002) 5647.
22. J. Douglas Jr., J. E. Santos and D. Sheen, Nonconforming Galerkin methods for the Helmholtz equation, *Numer. Methods Partial Diff. Eqs.* **17** (2001) 475.
23. C. L. Ravazzoli, J. Douglas Jr., J. E. Santos and D. Sheen, On the solution of the equations of motion for nearly elastic solids in the frequency domain, in *Anales de la* 4^a*. Reunión de Trabajo en Procesamiento de la Información y Control, RPIC '91, November 18–22, Buenos Aires*, 1991, pp. 231–235. Also, *Technical Report # 164, Center for Applied Mathematics, Purdue University*, (W. Lafayette, Indiana, 47907, 1991).
24. P. M. Gauzellino, J. E. Santos and D. Sheen, Frequency domain wave propagation modeling in exploration seismology, *J. Comput. Acoust.* **9** (2001) 941.
25. J. Douglas Jr., P. L. Paes Leme, J. E. Roberts and J. Wang, A parallel iterative procedure applicable to the approximate solution of second order partial differential equations by mixed finite element methods, *Numer. Math.* **65** (1993) 95.
26. J. Douglas Jr., J. E. Santos, D. Sheen and X. Ye, Nonconforming Galerkin methods based on quadrilateral elements for second order elliptic problems, *RAIRO Math. Modeling and Numer. Analysis* (*M2AN*) **33** (1999) 747.
27. P. A. Raviart and J. M. Thomas, Mixed finite element method for 2nd order elliptic problems, *Mathematical Aspects of the Finite Element Methods, Lecture Notes of Mathematics*, Vol. 606 (Springer, 1975).
28. J. C. Nedelec, Mixed finite elements in R^3, *Numer. Math.* **35** (1980) 315.
29. O. Kelder and D. Smeulders, Observation of the Biot slow wave in water-saturated Nivelsteiner sandstone, *Geophysics* **62** (1997) 1794.
30. J. Bear, *Dynamics of Fluids in Porous Media* (Dover Publications, New York, 1972).
31. D. W. Peaceman, *Fundamentals of Numerical Reservoir Simulation* (Elsevier, 1977).
32. A. E. Scheidegger, *The Physics of Flow Through Porous Media* (University of Toronto, Toronto, 1974).

33. H. P. Liu and D. L. Anderson and H. Kanamori, Velocity dispersion due to anelasticity; implications for seismology and mantle composition, *Geophys. J. R. Astr. Soc.* **l47** (1976) 41.
34. D. L. Johnston, J. Koplik and R. Dashen, Theory of dynamic permeability and tortuosity in fluid-saturated porous media, *J. Fluid Mechanics* **176** (1987) 379.
35. J. G. Berryman, Confirmation of Biot's theory, *Appl. Phys. Lett.* **37** (1980) 382.
36. J. E. Santos, J. M. Corberó, C. L. Ravazzoli and J. L. Hensley, Reflection and transmission coefficients in fluid saturated porous media, *J. Acoust. Soc. Amer.* **91** (1992) 1911.
37. J. L. Auriault, Nonsaturated deformable porous media: Quasistatics, *Transport in Porous Media* **2** (1987) 45.
38. J. L. Auriault, O. Lebaigue and G. Bonnet, Dynamics of two immiscible fluids flowing through deformable porous media, *Transport in Porous Media* **4** (1989) 105.
39. J. M. Hovem and G. D. Ingram, Viscous attenuation of sound in saturated sand, *J. Acoust. Soc. Amer.* **66** (1979) 1807.
40. D. Sheen, Finite element methods for an acoustic well-logging problem associated with a porous medium saturated by a two-phase immiscible fluid, *Numer. Methods for Partial Diff. Eqs.* **9** (1993) 155.
41. J. Douglas Jr., F. Furtado and F. Pereira, On the numerical simulation of waterflooding of heterogeneous petroleum reservoirs, *Comput. Geosciences* **1** (1997) 155.